Self-sustained elastoinertial Tollmien–Schlichting waves

**Ashwin Shekar[1], Ryan M. McMullen[2], Beverley J. McKeon[2]
and Michael D. Graham[1],†**

[1]Department of Chemical and Biological Engineering, University of Wisconsin–Madison,
Madison, WI 53706, USA

[2]Graduate Aerospace Laboratories, California Institute of Technology, Pasadena, CA 91125, USA

Direct simulations of two-dimensional plane channel flow of a viscoelastic fluid at Reynolds number $Re = 3000$ reveal the existence of a family of attractors whose structure closely resembles the linear Tollmien–Schlichting (TS) mode, and in particular exhibits strongly localized stress fluctuations at the critical layer position of the TS mode. At the parameter values chosen, this solution branch is not connected to the nonlinear TS solution branch found for Newtonian flow, and thus represents a solution family that is nonlinearly self-sustained by viscoelasticity. The ratio between stress and velocity fluctuations is in quantitative agreement for the attractor and the linear TS mode, and increases strongly with Weissenberg number, *Wi*. For the latter, there is a transition in the scaling of this ratio as *Wi* increases, and the *Wi* at which the nonlinear solution family comes into existence is just above this transition. Finally, evidence indicates that this branch is connected through an unstable solution branch to two-dimensional elastoinertial turbulence (EIT). These results suggest that, in the parameter range considered here, the bypass transition leading to EIT is mediated by nonlinear amplification and self-sustenance of perturbations that excite the TS mode.

---

1. Introduction

Adding minute quantities (parts per million) of long-chain polymer additives can dramatically change the turbulent flow of Newtonian fluids, the most significant consequence being the considerable drop in friction factor, which is commonly referred to as the Toms effect (Virk 1975; White & Mungal 2008; Graham 2014). Accompanying this overall change is a structural change to the flow. At high levels of viscoelasticity, Dubief, Terrapon & Soria (2013) and Samanta *et al.* (2013) have shown that trains of weak spanwise-oriented flow structures with inclined sheets of polymer stretch dominate the flow, denoting this regime as elastoinertial turbulence (EIT). These sheets of polymer stretch correspond to a layer near each wall of localized spanwise vortex motion. In further contrast to the three-dimensional

† Email address for correspondence: mdgraham@wisc.edu

(3-D) structures that sustain Newtonian turbulence, Sid, Terrapon & Dubief (2018) demonstrated that EIT is fundamentally two-dimensional (2-D) in nature by showing that the structures sustaining 2-D EIT in channel flow simulations are similar to those in three dimensions. In a computational study of EIT in pipe flow, Lopez, Choueiri & Hof (2019) also observe nearly 2-D spanwise vortices in the near-wall region, indicating the structural similarities between EIT in channels and pipes.

Choueiri, Lopez & Hof (2018) experimentally studied the path to EIT in pipe flow by varying polymer concentration at fixed Reynolds number, *Re*. For sufficiently low *Re*, they observed an initial drop in friction factor (i.e. modification of Newtonian turbulence) as concentration increased, followed by relaminarization and eventually by a re-entrant transition to EIT, where the flow had very different structure from Newtonian turbulence. These observations point at two distinct types of turbulence in dilute polymer solutions – one that is suppressed by viscoelasticity (Newtonian turbulence) and one that is promoted (EIT).

Shekar *et al.* (2019) corroborated this observation of a re-entrant transition to EIT in simulations of channel flow with increasing Weissenberg number, *Wi*, the ratio between the polymer relaxation time scale and the shear time scale. They further showed that, close to its inception, EIT exhibits localized polymer stress fluctuations that bear strong resemblance to critical layer structures predicted by linear analyses, i.e. sheetlike fluctuations localized at wall-normal locations where the disturbance wave speed equals the base flow velocity. In particular, they demonstrated that the fluctuation structure corresponding to the dominant spectral content strongly resembles the viscoelastic extension of the linear Tollmien–Schlichting (TS) wave. This is perhaps a surprising result, as the flow in the parameter regime considered is linearly stable, and in Newtonian turbulence the TS mode plays a very limited role. Some light is shed on this issue through resolvent analysis, i.e. determination of the response of the linearized dynamics to harmonic-in-time disturbances, which shows that the linear TS mode becomes highly amplified in the presence of viscoelasticity. This strong amplification implies that even very weak disturbances may be sufficient to trigger the nonlinear effects necessary to sustain EIT.

We note that similar structures have been observed by other researchers in different contexts. Page & Zaki (2015) analysed the evolution of vortical perturbations in 2-D viscoelastic simple shear flow. Their analysis reveals a viscoelastic analogue of the Newtonian Orr mechanism. This 'reverse-Orr' mechanism generates tilted sheets of polymer stress fluctuations resembling those seen at EIT and thus may play some role in this phenomenon.

Because prior work on EIT reveals structures similar to those seen in the linear TS mode, the present work focuses on TS waves, but in the fully nonlinear context of self-sustained solutions in the channel flow geometry. (In the parameter regime here, the laminar flow is always linearly stable.) After introducing the formulation and computational methods, we show how the Newtonian nonlinear TS wave branch is modified by viscoelasticity, resulting in its disappearance as *Wi* increases. At still higher *Wi*, however, we demonstrate the onset of a new, viscoelasticity-driven, nonlinear solution branch that strongly resembles the linear TS mode, and illustrate how it is related to the TS mode of linear theory and to EIT.

2. Formulation

This study focuses on 2-D pressure-driven channel flow with constant mass flux. The *x* and *y* axes are aligned with the streamwise and wall-normal directions, respectively.

Lengths are scaled by the half channel height l, so the dimensionless channel height $L_y = 2$. The domain is periodic in x with length L_x. Velocity $\boldsymbol{v}$ is scaled with the Newtonian laminar centreline velocity U, time t with l/U, and pressure p with ρU^2, where ρ is the fluid density. The polymer stress tensor $\boldsymbol{\tau}_p$ is related to the polymer conformation tensor $\boldsymbol{\alpha}$ through the FENE-P constitutive relation, which models each polymer molecule as a pair of beads connected by a nonlinear spring with maximum extensibility b.

We solve the momentum, continuity and FENE-P equations:

$$\frac{\partial \boldsymbol{v}}{\partial t} + \boldsymbol{v} \cdot \nabla \boldsymbol{v} = -\nabla p + \frac{\beta}{Re} \nabla^2 \boldsymbol{v} + \frac{(1-\beta)}{ReWi} (\nabla \cdot \boldsymbol{\tau}_p), \tag{2.1}$$

$$\nabla \cdot \boldsymbol{v} = 0, \tag{2.2}$$

$$\boldsymbol{\tau}_p = \frac{\boldsymbol{\alpha}}{1 - \dfrac{\mathrm{tr}(\boldsymbol{\alpha})}{b}} - \boldsymbol{I}, \tag{2.3}$$

$$\frac{\partial \boldsymbol{\alpha}}{\partial t} + \boldsymbol{v} \cdot \nabla \boldsymbol{\alpha} - \boldsymbol{\alpha} \cdot \nabla \boldsymbol{v} - (\boldsymbol{\alpha} \cdot \nabla \boldsymbol{v})^{\mathrm{T}} = \frac{-1}{Wi} \boldsymbol{\tau}_p. \tag{2.4}$$

Here $Re = \rho U l / (\eta_s + \eta_p)$, where η_s and η_p are the solvent and polymer contributions to the zero-shear-rate viscosity. The viscosity ratio $\beta = \eta_s/(\eta_s + \eta_p)$. We fix $\beta = 0.97$ and $b = 6400$. Since $1 - \beta$ is proportional to polymer concentration and b to the number of monomer units, this parameter set corresponds to a dilute solution of a high-molecular-weight polymer. The Weissenberg number $Wi = \lambda U/l$, where λ is the polymer relaxation time.

For the nonlinear direct numerical simulations (DNS) described below, a finite difference scheme and a fractional time-step method are adopted for integrating the Navier–Stokes equation. Second-order Adams–Bashforth and Crank–Nicolson methods are used for convection and diffusion terms, respectively. The FENE-P equation is discretized using a high-resolution central difference scheme (Kurganov & Tadmor 2000; Vaithianathan *et al.* 2006; Dallas, Vassilicos & Hewitt 2010) that guarantees positive definiteness of the polymer conformation tensor without the need for any artificial diffusion. In any case, the nonlinear solution branch on which we focus in this paper displays weak fluctuations far from the limit of positive definiteness even at the highest Wi of existence. A typical resolution for the following results is $(N_x, N_y) = (79, 402)$. This resolution used was based on mesh convergence results at $Wi = 45$. When the resolution was increased to $(N_x, N_y) = (131, 602)$, the mean polymer stretch deviations from the laminar base state change by less than 1 %.

We also consider the linearized evolution of infinitesimal perturbations to the laminar state with given streamwise wavenumber k. Two approaches are used. The first is classical linear stability analysis, in which solutions of the form $\hat{\boldsymbol{\phi}}(y) \exp[\mathrm{i}k(x-ct)]$ are sought, resulting in an eigenvalue problem for the complex wave speed c at a given k. In the present study, a hat $\hat{\ }$ always indicates deviation from the laminar state. If all $c_i < 0$, which is the case for all conditions considered in the present study, the flow is linearly stable. A linearized version of the DNS code was also developed using the numerical schemes described above. Results were validated against linear stability analysis, and agreement to three significant digits was obtained for the value of c for the viscoelastic TS mode at the parameters of interest.

The second linear approach used here determines the linear response of the laminar flow to external forcing with given wavenumber k and frequency ω using the resolvent

operator of the linearized equations (Schmid 2007; McKeon & Sharma 2010). The norm used in the resolvent calculations is

$$\|\hat{\boldsymbol{\phi}}\|_{\boldsymbol{A}}^2 = \int_{-1}^{1} [\hat{\boldsymbol{v}}^* \hat{\boldsymbol{v}} + \mathrm{tr}(\boldsymbol{A}^{-1} \hat{\boldsymbol{\alpha}}^* \boldsymbol{A}^{-1} \hat{\boldsymbol{\alpha}})] \, \mathrm{d}y, \tag{2.5}$$

where $\boldsymbol{A}$ is the conformation tensor in the laminar state. The second term provides a measure of the conformation tensor perturbation magnitude that is motivated by the non-Euclidean geometry of positive definite tensors (Hameduddin, Gayme & Zaki 2019). For both the linear stability and resolvent analyses, the equations are discretized with a Chebyshev pseudospectral method using 401 Chebyshev polynomials. This number was arrived at by ensuring convergence of the TS eigenvalue.

3. Results and discussion

3.1. *Origin of Newtonian and viscoelastic nonlinear Tollmien–Schlichting attractors*

In Newtonian flow, a family of nonlinear TS waves bifurcates subcritically from the laminar branch at $Re \approx 5772$ with $L_x \approx 2\pi/1.02 \approx 6.15$. The lower limit of the parameter regime for which this solution family exists is $Re \approx 2800$, $L_x \approx 2\pi/1.3 \approx 4.83$ (Jiménez 1990). Furthermore, in prior work on EIT (Shekar *et al.* 2019), as well as in more recent simulations in long 2-D domains, a strong peak in the spatial spectrum is found at $L_x \approx 5$. Based on these observations, all of the results presented in this study will be at $Re = 3000$, $L_x = 5$. (At $L_x = 5$, Newtonian channel flow is linearly stable at all Re.) In the Newtonian limit at these parameters, there are upper and lower branch solutions (which merge in a saddle-node bifurcation as Re is lowered); the upper branch travelling wave solution is linearly stable with respect to 2-D perturbations and is thus easily computed via DNS. We call this solution branch, including its viscoelastic extension, the Newtonian nonlinear Tollmien–Schlichting attractor (NNTSA). (The word 'attractor' is chosen rather than 'wave' because, depending on parameters, one can observe a pure travelling wave state or one with periodic or non-periodic modulations.)

On increasing Wi, the self-sustained nonlinear viscoelastic TS wave at $Re = 3000$ develops sheets of high polymer stretch that start out from near the wall. These observations are evidence of the capability of nonlinear TS critical layer mechanisms in generating sheets of polymer stretch. Figure 1 illustrates this point with a snapshot of $\hat{\alpha}_{xx}$ on the NNTSA branch at $Wi = 3$. The sheets originate in the nonlinear Kelvin cat's eye kinematics of TS waves at finite amplitude, as detailed in Shekar *et al.* (2019). The NNTSA continues to display wall-normal velocity fluctuations that extend across the channel centreline – a signature of TS kinematics. Some of the observations made in Shekar *et al.* (2019) are repeated here for completeness, as they form the background for the new results of the present study.

At the parameters chosen, the solution branch originating in the self-sustained Newtonian TS wave bifurcates to a periodic orbit at $Wi \approx 3.5$ (cf. Lee & Zaki 2017) before turning back into a travelling wave and losing existence beyond $Wi = 3.875$, evidently in a saddle-node bifurcation yielding a lower branch TS wave solution that becomes the Newtonian solution as $Wi \rightarrow 0$. Consistent with a saddle-node bifurcation, if the solution at $Wi = 3.875$ is used as an initial condition for a simulation at slightly higher Wi, the flow laminarizes. This bifurcation scenario is shown in figure 2(*a*) in terms of average wall shear rate versus Wi. The unstable lower branch (dashed blue) was found using edge tracking (Zammert & Eckhardt 2014) between NNTSA
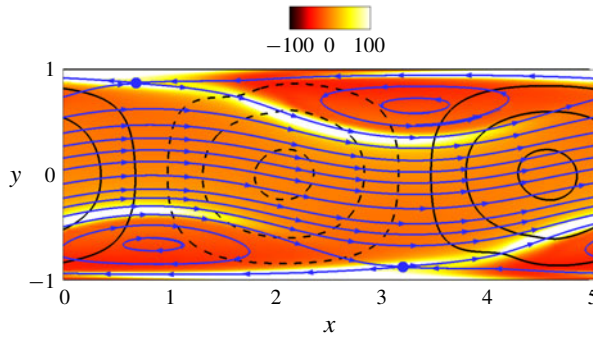
FIGURE 1. Structure of NNTSA at $Re = 3000$, $Wi = 3$. Streamlines (blue) in a reference frame moving at the wave speed $c = 0.39$ are superimposed on colour contours of $\hat{\alpha}_{xx}$, where the hat $\hat{}$ denotes deviations from the laminar state. Blue dots indicate the locations of hyperbolic stagnation points (in the travelling frame). Black contour lines of $\hat{v}$ are also shown. For $\hat{v}$, dashed = negative and solid = positive.
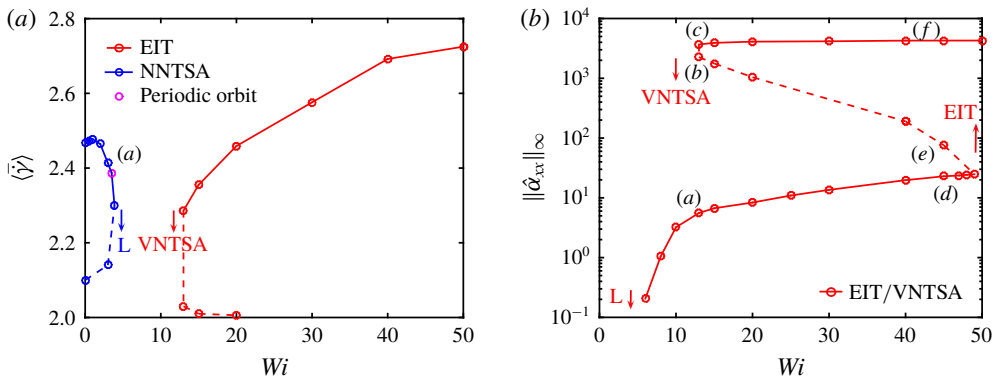

FIGURE 2. (a) Bifurcation diagram showing the evolution of the space- and time-averaged wall shear rate with Wi for the 2-D nonlinear NNTSA and EIT branches at $Re = 3000$, $L_x = 5$. Point (a) corresponds to the structure shown in figure 1. Labels 'L' and 'VNTSA' indicate that initial conditions starting at the arrows evolve to laminar or VNTSA states, respectively. (b) Bifurcation diagram of the L_∞-norm of $\hat{\alpha}_{xx}$ with Wi for VNTSA and EIT. Points (a)–(f) correspond to structures shown later in figure 6. The label 'EIT' indicates that initial conditions evolve to EIT. In both panels, dashed lines correspond to the unstable solution branches obtained from edge tracking.

and laminar solutions at a given Wi. A bisection technique was used to arrive at arbitrarily close initial conditions that are on either side of the edge. DNS trajectories starting from such points stay on the edge for a while before diverging to NNTSA and laminar.

As shown in Shekar *et al.* (2019), if Wi is large, sufficiently energetic initial conditions lead to 2-D EIT. Figure 2(a) also shows the mean wall shear rate for the EIT solution branch, which loses existence at finite amplitude when $Wi \lesssim 13$. The bifurcation underlying this transition is presumably also of saddle-node form.

The central observation of the present paper arises from considering what happens just below the onset of the EIT regime at $Wi \approx 13$. We do this by using a velocity and
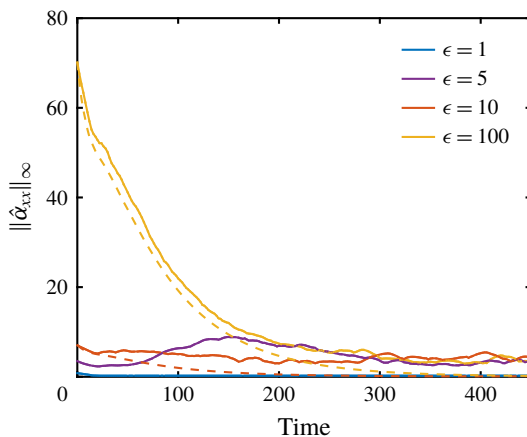
FIGURE 3. Time evolution of the L_∞-norm of $\hat{\alpha}_{xx}$ for $Re = 3000$, $Wi = 13$, $L_x = 5$, starting from an initial condition of laminar state $+ \ \epsilon \times$ TS-mode. Dashed lines correspond to linearized runs starting from the same initial conditions for $\epsilon = 10$ and 100.

stress field from EIT at $Wi = 13$ as an initial condition for a run at $Wi = 12$. This initial condition persists as a slowly decaying form of EIT for hundreds of time units (TU), consistent with behaviour just beyond a saddle-node bifurcation. As time increases further, the structure continues to decay, but does not ultimately reach the laminar state. Instead, it evolves to a non-trivial attractor state that is very nearly a travelling wave, and in particular strongly resembles the linear TS mode at these parameters. We call this new state the viscoelastic nonlinear Tollmien–Schlichting attractor (VNTSA).

3.2. *Viscoelastic nonlinear Tollmien–Schlichting attractor*

To elaborate on the relationship between the VNTSA and the linear TS mode, we describe results at $Re = 3000$, $Wi = 13$, $L_x = 5$, i.e. close to the point where the 2-D EIT branch first comes into existence as shown in the bifurcation diagram (figure 2a). EIT and the VNTSA are coexisting attractors at these parameter values. Figure 3 shows the evolution of the L_∞-norm of $\hat{\alpha}_{xx}$ starting from an initial condition consisting of the laminar state plus some amplitude ϵ of the linear TS mode for this parameter set. This mode, with $\epsilon = 1$, is shown in figure 4(a). The structure of the velocity field is virtually unchanged from the Newtonian case and the polymer conformations are strongly localized to the critical layer positions $y = \pm 0.82$. Sufficiently small perturbations, e.g. $\epsilon = 1$, decay to the laminar state, as they must since that state is linearly stable. However, for larger perturbations, $\epsilon = 5$, 10 and 100, where nonlinear mechanisms play a role, $\hat{\alpha}_{xx}$ settles to a finite value corresponding to the VNTSA. The initial condition $\epsilon = 5$ that starts from below the VNTSA in $\|\hat{\alpha}_{xx}\|_\infty$ shows an initial growth phase before saturating onto the VNTSA, whereas $\epsilon = 10$ and 100 relax onto the VNTSA from above.

For comparison, the dashed lines in figure 3 show the linearized evolution starting from the same initial conditions; these all decay to laminar, illustrating the role of nonlinearity in the transition to the VNTSA. This state is robust: initial perturbation amplitudes over a wide range will evolve to it. However, initial conditions with very large magnitudes (e.g. $\epsilon = 6000$) evolve to EIT: as noted above, both EIT and VNTSA are attractors at the chosen parameters (as is the laminar state).
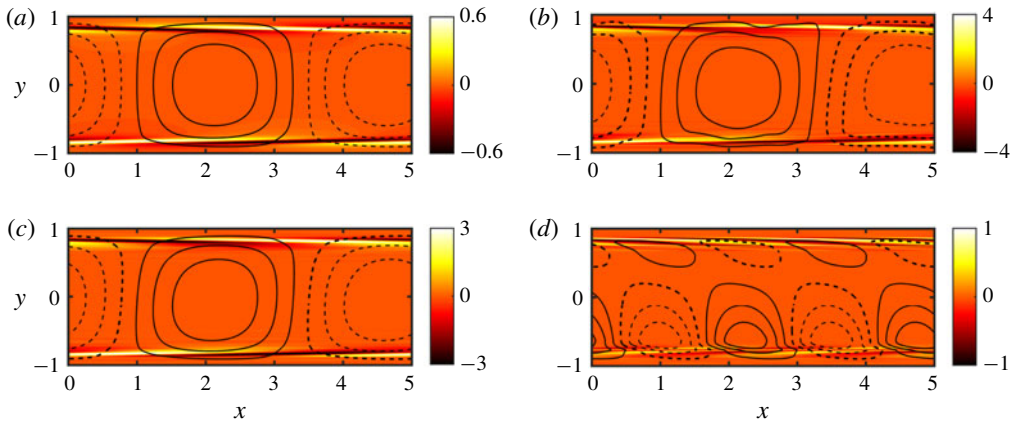
FIGURE 4. (*a*) Structure of the linear TS mode at $Re = 3000$, $Wi = 13$, $L_x = 5$. Magnitude of the eigenmode is arbitrary and values shown here correspond to $\epsilon = 1$. (*b*) Snapshot of the fluctuation structure of the VNTSA at $Re = 3000$, $Wi = 13$. (*c*,*d*) The $kL_x/2\pi = 1$, 2 components, respectively, of the snapshot shown in (*b*). Shown are contour lines of $\hat{v}$ superimposed on colour contours of $\hat{\alpha}_{xx}$.

We have also used initial conditions of the laminar state plus velocity perturbations somewhat similar to the ones used by Page & Zaki (2015). These perturbations satisfied incompressibility and were sinusoidal in nature, with streamwise and wall-normal periods equal to the domain size. When appropriate magnitudes are used, transient growth of polymer stress followed by a decay to the VNTSA is observed.

In 3-D channel flow simulations of Oldroyd-B fluids at $Re = 3000$, $Wi = 4$–6, $\beta = 0.9$, Min, Choi & Yoo (2003) observe a transient ($\sim$500 TU) before an abrupt jump to the fully developed state. These observations were made starting from turbulent Newtonian initial conditions. In the present work, we used an average of approximately 2500 TU of data, and in some cases more than 5000 TU to calculate the statistics, and have observed no similar transition in any simulations of VNTSA in the parameter space considered here.

Figure 4(*b*) is a snapshot showing the typical fluctuation structure of the VNTSA at $Wi = 13$. The streamwise conformation $\hat{\alpha}_{xx}$ has tilted sheets highly localized near $y = \pm 0.82$, and contours of wall-normal velocity $\hat{v}$ span the entire channel. This structure bears strong resemblance to the TS mode shown in figure 4(*a*). The VNTSA is thus a weakly nonlinear self-sustaining state whose primary structure is the viscoelastic TS mode. We elaborate in the following section on the linear TS mode and its connections to the VNTSA.

In the VNTSA state, the velocity fluctuations are very weak, and the mean wall shear rate displays a very small change from laminar. This can be understood on the grounds that changes of the mean wall shear rate correspond to fluctuations with $k = 0$, which arise only due to nonlinear interactions. Since the primary velocity structure is very weak, the nonlinear effects will be even weaker. To illustrate nonlinear effects, figures 4(*c*) and 4(*d*), respectively, show the $kL_x/2\pi = 1$ and 2, spatial Fourier components of the snapshot shown in figure 4(*b*). Figure 4(*c*) closely resembles the TS mode, with a slight symmetry breaking across the centreline $y = 0$. The structure at $kL_x/2\pi = 2$ also displays polymer stress fluctuations localized around the critical layer position, an observation that also holds for higher wavenumbers.

Having established the structure of the flow on the VNTSA branch, we now illustrate the bifurcation scenario of this solution branch by continuing in *Wi*. The VNTSA branch loses existence at finite amplitude (i.e. in a saddle-node bifurcation) for $Wi \lesssim 6$, as we have confirmed both by using the $Wi = 6$ solution as an initial condition for simulations at lower *Wi* and by running simulations starting from the laminar state perturbed by the TS mode with small ϵ. For $Wi < 6$ all these initial conditions decay to laminar. On increasing *Wi*, the VNTSA branch seems to lose existence beyond $Wi \approx 49$, and initial conditions that land on the VNTSA for $Wi = 49$ evolve to EIT at $Wi = 50$. Due to its weak nature in relation to EIT, the bifurcation scenario associated with the two solution branches is shown in figure 2(*b*) in a log scale using the L_∞-norm of $\hat{\alpha}_{xx}$ as the amplitude measure. The EIT solutions in figure 2(*a*) are depicted again in figure 2(*b*) as the upper stable branch (solid red) with this measure.

Since the VNTSA and EIT are both stable states, we were also able to perform edge tracking to find unstable solutions intermediate between these two states. Five *Wi* values (13, 15, 20, 40 and 45) were studied. Repeated bisections were performed until trajectories stayed on the edge for an average of 300 TU. The red dashed line in figure 2(*a,b*) indicates solutions (all time-dependent) on this intermediate branch. The magnitude of fluctuations along this branch monotonically decreases on increasing *Wi*, displaying values close to EIT at $Wi = 13$ and values to close to VNTSA at $Wi = 45$. Furthermore, this branch also displays fluctuations that resemble the viscoelastic TS mode, as illustrated below. A more detailed link between VNTSA and EIT might be established through numerical continuations of underlying travelling wave solutions; this is a topic of future endeavours.

To complete this discussion, we note that the bifurcation scenario we observe implies the existence of an edge between the VNTSA and the laminar state, which could in principle also be found using edge tracking. However, the weak nature of the VNTSA implies that this edge would be even weaker, thus making this a challenging task.

Figure 5(*a*) shows the fluctuation structure of the VNTSA at $Wi = 8$, close to the point where it first comes into existence. The structure closely resembles the TS mode and does not change appreciably with time. The flow is almost a pure nonlinear travelling wave with some weak non-periodicity, as indicated in the power density plot of the wall-normal velocity at position (0, 0.825) shown in figure 5(*b*). The spectrum is mainly composed of the dominant TS mode frequency and its higher harmonics. The dynamics and structures get more complicated as *Wi* increases. Figure 5(*c*) shows a typical snapshot at $Wi = 20$, which clearly is more complex than a TS mode. However, at this *Wi*, the VNTSA still intermittently displays clear TS-like structures, such as the snapshot in figure 5(*d*).

We now turn to the flow structures at various positions on the bifurcation diagram, figure 2(*b*). Figures 6(*a*), 6(*b*) and 6(*c*) are representative snapshots of VNTSA, the intermediate branch and EIT, respectively, at $Wi = 13$, i.e. near the loss of existence of EIT. As detailed in the description of figure 4 and shown again in figure 6(*a*), VNTSA exhibits a weak structure that strongly resembles the viscoelastic TS mode. At this low *Wi*, the intermediate branch (figure 6*b*) displays a much stronger fluctuation structure, of the same order of magnitude as the structures seen at EIT (figure 6*c*). Moreover, the intermediate branch exhibits overlapping sheets of polymer stretch (especially on the bottom side of the channel at the time instant shown) that strongly resemble those seen at EIT.
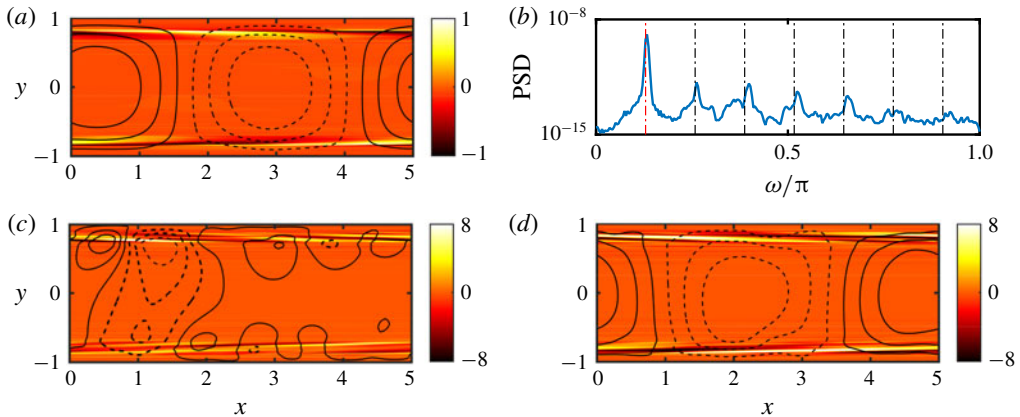
FIGURE 5. (*a*) Fluctuation structure of the VNTSA and (*b*) power spectral density (PSD) of *v* at position $(0, 0.825)$ at $Re = 3000$, $Wi = 8$. Frequencies corresponding to the TS mode (red dashed) and its higher harmonics (black dashed) are also shown. (*c*,*d*) Snapshots of the VNTSA structure for $Re = 3000$, $Wi = 20$. Contour plots follow the same format as in figure 4.

Figure 6(*d–f*) show the structures at $Wi = 45$, close to the point where the intermediate branch seems to turn around to merge with VNTSA. The fluctuations on the intermediate branch (figure 6*e*) decrease in magnitude on increasing Wi, and at $Wi = 45$ become comparable to those on the VNTSA branch as shown in figure 6(*d*). Furthermore, the structure on this branch goes from displaying overlapping sheets of polymer stretch at low Wi to localized striations at high Wi similar to those of VNTSA. In sharp contrast to the localized structures just described, EIT (figure 6*f*) continues to display sheets of polymer stretch, which get stronger on increasing Wi. All three solution branches continue to intermittently display wall-normal velocity fluctuations that resemble the TS mode.

3.3. *Linear analyses*

In this section we elaborate on the linearized problem and its connection to the attractors described above using linear stability and resolvent analyses. The spectrum corresponding to disturbances with wavelengths equal to the DNS box size, i.e. $k = 2\pi/5$, has a least stable eigenvalue at $c \approx 0.32–0.010i$, and the associated eigenfunction is the viscoelastic extension of the TS mode. For low values of Wi, the mode is less stable than its Newtonian counterpart, while for $Wi \gtrsim 2$, it becomes more stable with increasing elasticity. This non-monotonic behaviour has been reported by Zhang *et al.* (2013), who attribute it to viscoelastic modification of the phase difference between *u* and *v*. Nevertheless, over the range of Wi considered here, the eigenvalue varies by less than 1 % of the Newtonian value. The linear stability of the laminar state in this range of Wi, and the very weak dependence of *c* on Wi, continues up to at least $Re = 6000$, confirming the observations in § 3.2 that finite-amplitude disturbances are required to trigger transition to EIT or the VNTSA. However, linear instabilities not related to the TS mode have been found in other regions of parameter space (Garg *et al.* 2018; Chaudhary *et al.* 2019), implying the possibility of different attractor families in those regions.
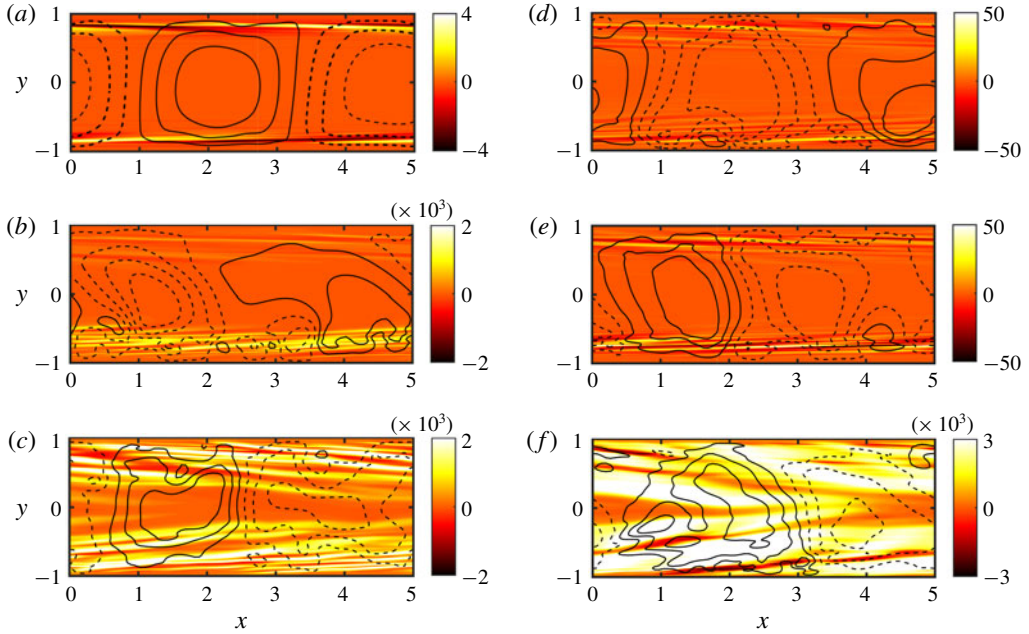
FIGURE 6. (*a–c*) Snapshots of VNTSA, intermediate branch and EIT respectively at $Wi = 13$. (*d–f*) Snapshots of the same solution branches at $Wi = 45$. Deviations from the laminar base state shown as earlier. Colour scales are intentionally centred about 0 for comparison purposes.
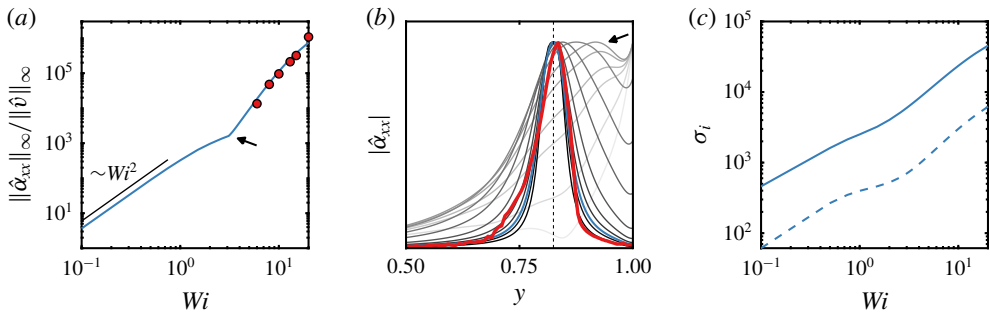

FIGURE 7. (*a*) Solid blue line: ratio of peak amplitudes of $\hat{\alpha}_{xx}$ and $\hat{v}$ for the linear TS mode as a function of Wi. Circles: amplitude ratio for the VNTSA. (*b*) Magnitude of $\hat{\alpha}_{xx}$ for the linear TS mode for several values of Wi in the range $[1, 20]$. Darker lines indicate higher values of Wi. The thick red line shows the averaged magnitude of $\hat{\alpha}_{xx}$ from the VNTSA for $Wi = 13$. For comparison, the linear TS mode profile for the same Wi is shown in blue, and the vertical dashed line marks the critical layer location $y_c = 0.825$. The arrow indicates the value of Wi corresponding to the arrow in (*a*). (*c*) First two singular values of the resolvent operator for k and c corresponding to the linear TS mode.

A measure of the relative importance of the conformation tensor and velocity disturbances is the ratio of the peak amplitudes of $\hat{\alpha}_{xx}$ (the largest component of the conformation tensor) and $\hat{v}$. This ratio is shown in figure 7(*a*). Two distinct

regimes are apparent, with the transition between the two occurring at $Wi \approx 3.1$. The low-Wi regime scales as Wi^2, which is the same scaling as in linear shear flow. The amplitude ratio above the change in slope does not exhibit power-law scaling. The change in slope at $Wi \approx 3.1$ can be understood by examining the $\hat{\alpha}_{xx}$ mode shapes, the magnitudes of which are plotted in figure 7(*b*) for several values of Wi in the range shown in figure 7(*a*). For small Wi, the disturbance is largest at the wall and decays rapidly away from it. Therefore, the Wi^2 scaling in this regime can be explained by the fact that the leading-order approximation of the base flow very near the wall is simple shear. As Wi increases, this value decreases, while a new local maximum emerges and grows, becoming the global maximum just above $Wi = 3$; the arrow in the figure indicates the profile where this occurs. Upon further increase in Wi, the maximum gradually shifts away from the wall, and the modes become increasingly localized around the location of the critical layer y_c, at which the real part of the wave speed equals the base flow velocity. The critical layer for $Wi = 13$ is indicated by the vertical dashed line. This suggests that a critical layer mechanism is responsible for the change in scaling at large Wi, though at present we do not understand the specific origin of this result. Interestingly, the Wi at which the VNTSA comes into existence is only slightly larger than that at which the transition to critical layer scaling occurs.

Also shown in figure 7(*a*) is the amplitude ratio computed from the VNTSA for several values of Wi. Excellent agreement between the linear and nonlinear results quantitatively reinforces the TS-mode-like nature of the VNTSA. Additionally, the profile of $|\hat{\alpha}_{xx}|$, averaged in the streamwise direction and over many snapshots, for the VNTSA at $Wi = 13$ is shown by the thick red line in figure 7(*b*), and the blue line highlights the linear mode for the same Wi. The VNTSA profile exhibits the same localization, and the location of the peak value is in close agreement with the critical layer location.

Figure 7(*c*) shows the first two singular values of the resolvent operator for k and c corresponding to the linear TS mode. Shekar *et al.* (2019) showed that such modes are the most-amplified 2-D disturbances in this parameter regime and that the leading response mode is nearly identical to the TS eigenmode; for this reason the resolvent modes are not plotted separately. The substantial increase in the leading singular value with Wi indicates that this amplification becomes much stronger with increasing elasticity, and consequently that considerably smaller disturbances may be sufficient to trigger self-sustaining nonlinear mechanisms. Further, the symmetry of the flow geometry about $y = 0$ means that resolvent modes typically come in pairs having similar amplification, with one mode having a symmetric $\hat{v}$ response and the other having an antisymmetric $\hat{v}$ response. However, the growing separation between the first and second singular values with increasing Wi indicates that this pairing is broken by elasticity, and that the symmetry exhibited by the TS mode is preferred in terms of linear amplification.

3.4. *Broader context: flow geometry and dimensionality*

The results described above are limited to 2-D channel flow. Here we describe how they may be viewed in the broader context of turbulent drag reduction, first with regard to how they may relate to the pipe flow geometry and then in the full context of 3-D turbulence.

As noted in the introduction, EIT with very similar features has been observed in both channel and pipe flows. A natural question, then, is to what extent the above

channel flow results are relevant to the pipe flow case. While it is true, of course, that there is no linear instability of Newtonian pipe flow, the general structures of the linear stability problem for the pipe and channel are very similar. The A, P and S (wall, centre, strongly decaying) families of modes for the channel flow problem also arise in the pipe, as illustrated in figures 4.18 and 4.19 of Drazin & Reid (2004). (In channel flow, one of the wall modes, the TS mode, goes unstable.) Additionally, critical layers are a strong source of linear amplification in pipe flow, as they are in channel flow (McKeon & Sharma 2010).

Turning to nonlinear behaviour in Newtonian pipe flow, an important difference from channel flow is the apparent absence of subcritical travelling wave solutions that are analogous to the nonlinear TS waves (Patera & Orszag 1981). That is, in pipe flow there is no nonlinear solution branch that corresponds to the NNTSA described above. Given this observation, one might wonder whether the results presented here for viscoelastic channel flow are relevant for pipe flow.

To address this issue, we make the following remarks. The key observation of the present work is that the TS mode is nonlinearly excited by viscoelasticity. The resulting solution branch, the VNTSA, is not connected, at least in this part of parameter space under consideration, to the Newtonian branch, indicating that the nonlinear mechanism that sustains it is distinct from the nonlinear mechanisms sustaining the Newtonian branch. So the absence of a Newtonian mechanism for nonlinear sustainment of TS-like travelling waves does not imply the absence of a viscoelastic mechanism. Furthermore, as noted in the introduction, pipe flow simulations of EIT (Lopez *et al.* 2019) display essentially 2-D velocity fluctuations localized near the wall that are similar to those reported in channel flow. These are precisely what would be expected in pipe flow based on the observations we report here for channel flow, i.e. a critical layer mechanism associated with excitation of a TS-like mode. At the same time, in more strongly viscoelastic regimes, Garg *et al.* (2018) and Chaudhary *et al.* (2020) have found a centre mode instability for pipe flow; for the Oldroyd-B model with $Re = 3500$, $\beta = 0.9$, instability occurs when $176.9 < Wi < 4783.6$. A related instability might be present in the channel flow problem. These results open up the possibility that other states unrelated to the nonlinear excitation of a wall mode may also play a role at EIT in both channels and pipes, especially at high Wi.

We now turn to the topic of how the present results are related to the fully 3-D context, beginning with a brief overview of Newtonian near-wall turbulence.

Newtonian turbulence is, of course, strongly 3-D, with the dominant near-wall structure composed of coherent wavy streamwise vortices. In all of the canonical wall-bounded shear flow geometries (pipe flow, channel flow, plane shear (Couette) flow), families of 3-D nonlinear travelling wave solutions to the Navier–Stokes equations have been discovered (Waleffe 1998, 2001, 2003; Hof *et al.* 2004; Wedin & Kerswell 2004; Wang, Gibson & Waleffe 2007; Eckhardt *et al.* 2007, 2008; Duguet, Willis & Kerswell 2008*b*). These solutions are often denoted 'exact coherent states' (ECS), and their predominant structure is very similar to that observed in wall turbulence: a mean shear and wavy streamwise vortices. (In particular, they bear no structural resemblance to TS waves and do not arise from a linear instability of the laminar state.) Related, but more complex, states have been found as well, which are not pure travelling waves but rather 'relative periodic orbits' that are time-periodic modulo a phase shift in one of the translation-invariant spatial directions (Duguet, Pringle & Kerswell 2008*a*). In minimal domains at Reynolds numbers near transition,

the turbulent dynamics has been found to be organized, at least in part, around these solutions (see e.g. Gibson, Halcrow & Cvitanović 2008, Kawahara, Uhlmann & van Veen 2012, Park & Graham 2015).

It has long been known that one of the effects of viscoelasticity on wall turbulence is to weaken and broaden the near-wall streamwise vortices (Kim *et al.* 2007; White & Mungal 2008). A number of studies have addressed this observation by investigating the effect of viscoelasticity on ECS, which, as noted, capture this streamwise vortex structure (Stone, Waleffe & Graham 2002; Stone & Graham 2003; Stone *et al.* 2004; Li, Stone & Graham 2005; Li, Xi & Graham 2006; Li & Graham 2007). Indeed, the effect of viscoelasticity is to weaken these structures; the polymer stresses directly counteract the streamwise vortices.

In particular, Li & Graham (2007) studied the bifurcation scenario for a particular family of channel flow ECS (Waleffe 1998) in a parameter regime very close to that considered here. At $Re = 1500$, this ECS family is sufficiently weakened by viscoelasticity to lose existence at $Wi \approx 16$, somewhat above the value $Wi \approx 10$ beyond which Newtonian turbulence cannot self-sustain in the DNS study of Shekar *et al.* (2019). (This discrepancy is consistent with what we know about transition in the Newtonian case: channel flow turbulence is self-sustaining above $Re \approx 1000$, while ECS can exist in that case down to $Re \approx 660$ (Shekar & Graham 2018).) Extrapolating slightly from the results of Li & Graham (2007), one can estimate that, at $Re = 3000$, this ECS family loses existence at $Wi \approx 25$.

Given that, in the present 2-D work with $Re = 3000$, EIT is found at $Wi \gtrsim 13$ and the VNTSA above at $Wi \gtrsim 6$, there would appear to be a regime $6 \lesssim Wi \lesssim 25$ in which both 2-D and 3-D structures may exist and interact. Furthermore, existing results on the effect of viscoelasticity on ECS are limited to one ECS family, and there certainly may be others that can persist to higher Wi. Consistent with this analysis, a number of studies have reported near-wall EIT-like spanwise-oriented structures, with 3-D quasi-streamwise vortices further away from the wall (Dubief *et al.* 2013; Choueiri *et al.* 2018; Pereira, Thompson & Mompean 2019*a,b*). How the 2-D and 3-D structures interact is an important topic for future work.

4. Conclusion

This study focuses on 2-D plane channel flow of a very dilute polymer solution at $Re = 3000$. At sufficiently high Wi, elastoinertial turbulence (EIT) is observed in this parameter regime, and the focus of the present work is to make progress towards understanding the structures and mechanisms underlying the dynamics in this regime. We report here the existence of a new attractor that is based on the viscoelastic linear Tollmien–Schlichting (TS) mode and is nonlinearly sustained by viscoelastic stresses. We denote this as the viscoelastic nonlinear Tollmien–Schlichting attractor (VNTSA). At the parameters considered here, this solution branch is not connected to the Newtonian branch of nonlinear self-sustained TS waves; it would be interesting to learn whether they become connected at higher Re. In a domain of dimensionless length 5, this solution comes into existence at finite but very small amplitude when $Wi \gtrsim 6$, increasing in amplitude until $Wi \approx 49$, where it loses existence again. At higher Wi, initial conditions corresponding to this solution branch at lower Wi evolve into EIT. In general, we do not find pure nonlinear travelling waves, but until Wi is large, the non-periodic fluctuations are very small. The connection of the VNTSA to the linear TS mode is established via their strong structural similarities, including a quantitative agreement between the relative magnitudes of the velocity

and stress fluctuations. The value of *Wi* at which the VNTSA comes into existence is close to where the relative amplitude of the stress and velocity fluctuations for the linear TS mode undergoes a change in scaling. Above this transition, the stress fluctuations become highly localized at the position of the critical layer.

Taken together, these results suggest that, at least in the parameter range considered here, the bypass transition leading to EIT is mediated by nonlinear amplification and self-sustenance of perturbations that excite the TS mode. Gaining an understanding of the mechanism underlying this phenomenon will shed light on the origin of EIT.

Acknowledgements

Declaration of interests

The authors report no conflict of interest.

REFERENCES

CHAUDHARY, I., GARG, P., SHANKAR, V. & SUBRAMANIAN, G. 2019 Elastoinertial wall mode instabilities in viscoelastic plane Poiseuille flow. *J. Fluid Mech.* **881**, 119–163.

CHAUDHARY, I., GARG, P., SUBRAMANIAN, G. & SHANKAR, V. 2020 Linear instability of viscoelastic pipe flow. *Preprint*, arXiv:2003.09369v1.

CHOUEIRI, G. H., LOPEZ, J. M. & HOF, B. 2018 Exceeding the asymptotic limit of polymer drag reduction. *Phys. Rev. Lett.* **120** (12), 124501.

DALLAS, V., VASSILICOS, J. & HEWITT, G. 2010 Strong polymer-turbulence interactions in viscoelastic turbulent channel flow. *Phys. Rev. E* **82** (6), 066303.

DRAZIN, P. G. & REID, W. H. 2004 *Hydrodynamic Stability*, 2nd edn. Cambridge Mathematical Libraries. Cambridge University Press.

DUBIEF, Y., TERRAPON, V. E. & SORIA, J. 2013 On the mechanism of elastoinertial turbulence. *Phys. Fluids* **25** (11), 110817.

DUGUET, Y., PRINGLE, C. C. T. & KERSWELL, R. R. 2008*a* Relative periodic orbits in transitional pipe flow. *Phys. Fluids* **20** (11), 114102.

DUGUET, Y., WILLIS, A. P. & KERSWELL, R. R. 2008*b* Transition in pipe flow: the saddle structure on the boundary of turbulence. *J. Fluid Mech.* **613**, 255–274.

ECKHARDT, B., FAISST, H., SCHMIEGEL, A. & SCHNEIDER, T. M. 2008 Dynamical systems and the transition to turbulence in linearly stable shear flows. *Phil. Trans. R. Soc. Lond.* A **366** (1868), 1297–1315.

ECKHARDT, B., SCHNEIDER, T. M., HOF, B. & WESTERWEEL, J. 2007 Turbulence transition in pipe flow. *Annu. Rev. Fluid Mech.* **39**, 447–468.

GARG, P., CHAUDHARY, I., KHALID, M., SHANKAR, V. & SUBRAMANIAN, G. 2018 Viscoelastic pipe flow is linearly unstable. *Phys. Rev. Lett.* **121** (2), 024502.

GIBSON, J. F., HALCROW, J. & CVITANOVIĆ, P. 2008 Visualizing the geometry of state space in plane Couette flow. *J. Fluid Mech.* **611**, 107–130.

GRAHAM, M. D. 2014 Drag reduction and the dynamics of turbulence in simple and complex fluids. *Phys. Fluids* **26**, 101301.

HAMEDUDDIN, I., GAYME, D. F. & ZAKI, T. A. 2019 Perturbative expansions of the conformation tensor in viscoelastic flows. *J. Fluid Mech.* **858**, 377–406.

HOF, B., VAN DOORNE, C. W. H., WESTERWEEL, J., NIEUWSTADT, F. T. M., FAISST, H., ECKHARDT, B., WEDIN, H., KERSWELL, R. R. & WALEFFE, F. 2004 Experimental observation of nonlinear traveling waves in turbulent pipe flow. *Science* **305** (5690), 1594–1598.

JIMÉNEZ, J. 1990 Transition to turbulence in two-dimensional Poiseuille flow. *J. Fluid Mech.* **218**, 265–297.

KAWAHARA, G., UHLMANN, M. & VAN VEEN, L. 2012 The significance of simple invariant solutions in turbulent flows. *Annu. Rev. Fluid Mech.* **44**, 203–225.

KIM, K., LI, C.-F., SURESHKUMAR, R., BALACHANDAR, S. & ADRIAN, R. J. 2007 Effects of polymer stresses on eddy structures in drag-reduced turbulent channel flow. *J. Fluid Mech.* **584**, 281–299.

KURGANOV, A. & TADMOR, E. 2000 New high-resolution central schemes for nonlinear conservation laws and convection–diffusion equations. *J. Comput. Phys.* **160** (1), 241–282.

LEE, S. J. & ZAKI, T. A. 2017 Simulations of natural transition in viscoelastic channel flow. *J. Fluid Mech.* **820**, 232–262.

LI, W. & GRAHAM, M. D. 2007 Polymer induced drag reduction in exact coherent structures of plane Poiseuille flow. *Phys. Fluids* **19** (8), 083101.

LI, W., STONE, P. A. & GRAHAM, M. D. 2005 Viscoelastic nonlinear traveling waves and drag reduction in plane Poiseuille flow. *Fluid Mech. Appl.: Proceedings of the IUTAM Symposium on Laminar-Turbulent Transition and Finite Amplitute Solutions* **77**, 285–308.

LI, W., XI, L. & GRAHAM, M. D. 2006 Nonlinear travelling waves as a framework for understanding turbulent drag reduction. *J. Fluid Mech.* **565**, 353–362.

LOPEZ, J. M., CHOUEIRI, G. H. & HOF, B. 2019 Dynamics of viscoelastic pipe flow at low Reynolds numbers in the maximum drag reduction limit. *J. Fluid Mech.* **874**, 699–719.

MCKEON, B. J. & SHARMA, A. S. 2010 A critical-layer framework for turbulent pipe flow. *J. Fluid Mech.* **658**, 336–382.

MIN, T., CHOI, H. & YOO, J. Y. 2003 Maximum drag reduction in a turbulent channel flow by polymer additives. *J. Fluid Mech.* **492**, 91–100.

PAGE, J. & ZAKI, T. A. 2015 The dynamics of spanwise vorticity perturbations in homogeneous viscoelastic shear flow. *J. Fluid Mech.* **777**, 327–363.

PARK, J. S. & GRAHAM, M. D. 2015 Exact coherent states and connections to turbulent dynamics in minimal channel flow. *J. Fluid Mech.* **782**, 430–454.

PATERA, A. T. & ORSZAG, S. A. 1981 Finite-amplitude stability of axisymmetric pipe flow. *J. Fluid Mech.* **112**, 467–474.

PEREIRA, A., THOMPSON, R. L. & MOMPEAN, G. 2019*a* Beyond the maximum drag reduction asymptote: the pseudo-laminar state. *Preprint*, arXiv:1911.00439.

PEREIRA, A. S., THOMPSON, R. L. & MOMPEAN, G. 2019*b* Common features between the Newtonian laminar–turbulent transition and the viscoelastic drag-reducing turbulence. *J. Fluid Mech.* **877**, 405–428.

SAMANTA, D., DUBIEF, Y., HOLZNER, M., SCHÄFER, C., MOROZOV, A. N., WAGNER, C. & HOF, B. 2013 Elastoinertial turbulence. *Proc. Natl Acad. Sci. USA* **110** (26), 10557–10562.

SCHMID, P. J. 2007 Nonmodal stability theory. *Annu. Rev. Fluid Mech.* **39**, 129–162.

SHEKAR, A. & GRAHAM, M. D. 2018 Exact coherent states with hairpin-like vortex structure in channel flow. *J. Fluid Mech.* **849**, 76–89.

SHEKAR, A., MCMULLEN, R. M., WANG, S.-N., MCKEON, B. J. & GRAHAM, M. D. 2019 Critical-layer structures and mechanisms in elastoinertial turbulence. *Phys. Rev. Lett.* **122** (12), 124503.

SID, S., TERRAPON, V. E. & DUBIEF, Y. 2018 Two-dimensional dynamics of elastoinertial turbulence and its role in polymer drag reduction. *Phys. Rev. F* **3** (1), 011301.

STONE, P. A. & GRAHAM, M. D. 2003 Polymer dynamics in a model of the turbulent buffer layer. *Phys. Fluids* **15** (5), 1247–1256.

STONE, P. A., WALEFFE, F. & GRAHAM, M. D. 2002 Toward a structural understanding of turbulent drag reduction: nonlinear coherent states in viscoelastic shear flows. *Phys. Rev. Lett.* **89** (20), 208301.

STONE, P. A., ROY, A., LARSON, R. G., WALEFFE, F. & GRAHAM, M. D. 2004 Polymer drag reduction in exact coherent structures of plane shear flow. *Phys. Fluids* **16** (9), 3470–3482.

VAITHIANATHAN, T., ROBERT, A., BRASSEUR, J. G. & COLLINS, L. R. 2006 An improved algorithm for simulating three-dimensional, viscoelastic turbulence. *J. Non-Newtonian Fluid Mech.* **140** (1–3), 3–22.

VIRK, P. S. 1975 Drag reduction fundamentals. *AIChE J.* **21** (4), 625–656.

WALEFFE, F. 1998 Three-dimensional coherent states in plane shear flows. *Phys. Rev. Lett.* **81** (19), 4140–4143.

WALEFFE, F. 2001 Exact coherent structures in channel flow. *J. Fluid Mech.* **435**, 93–102.

WALEFFE, F. 2003 Homotopy of exact coherent structures in plane shear flows. *Phys. Fluids* **15** (6), 1517–1534.

WANG, J., GIBSON, J. & WALEFFE, F. 2007 Lower branch coherent states in shear flows: transition and control. *Phys. Rev. Lett.* **98** (20), 204501.

WEDIN, H. & KERSWELL, R. R. 2004 Exact coherent structures in pipe flow: travelling wave solutions. *J. Fluid Mech.* **508**, 333–371.

WHITE, C. M. & MUNGAL, M. G. 2008 Mechanics and prediction of turbulent drag reduction with polymer additives. *Annu. Rev. Fluid Mech.* **40**, 235–256.

ZAMMERT, S. & ECKHARDT, B. 2014 Streamwise and doubly-localised periodic orbits in plane Poiseuille flow. *J. Fluid Mech.* **761**, 348–359.

ZHANG, M., LASHGARI, I., ZAKI, T. A. & BRANDT, L. 2013 Linear stability analysis of channel flow of viscoelastic Oldroyd-B and FENE-P fluids. *J. Fluid Mech.* **737**, 249–279.